

Epitaxial thin films of binary Eu-compounds close to a valence transition

Sebastian Kölsch*, Alfons Schuck, Michael Huth

Thin films and nanostructures, Physical Institute, Goethe University Frankfurt,
Max-von-Laue Street 1, Frankfurt am Main 60438, Germany

Abstract

Intermetallic binary compounds of europium reveal a variety of interesting phenomena due to the interconnection between two different magnetic and 4f electronic (valence) states, which are particularly close in energy. The valence states or magnetic properties are thus particularly sensitive to strain-tuning in these materials. Consequently, we grew epitaxial EuPd_2 (magnetic Eu^{2+}) and EuPd_3 (nonmagnetic Eu^{3+}) thin films on $\text{MgO}(001)$ substrates using molecular beam epitaxy. Ambient X-ray diffraction confirms an epitaxial relationship of cubic Laves-type (C15) EuPd_2 with an (111)-out-of-plane orientation, whereby eight distinct in-plane crystallographic domains develop. For simple cubic EuPd_3 two different out-of-plane orientations can be obtained by changing the substrate annealing temperature under ultra-high vacuum conditions from 600 °C to 1000 °C for one hour. A small resistance minimum evolves for EuPd_3 thin films grown with low temperature substrate annealing, which was previously found even in single crystals of EuPd_3 and might be attributed to a Kondo or weak localization effect. Absence of influence of an applied magnetic fields and magnetotransport measurements suggest a nonmagnetic ground state for EuPd_3 thin films, i.e., a purely trivalent Eu valence, as found in EuPd_3 single crystals. For EuPd_2 magnetic ordering below ~ 72 K is observed, quite similar to single crystal behavior. Field dependent measurements of the magnetoresistance and the Hall effect show hysteresis effects below ~ 0.4 T and an anomalous Hall effect below ~ 70 K, which saturates around 1.4 T, thus proving a ferromagnetic ground state of the divalent Eu.

1 Introduction

Intermetallic binary and ternary compounds of europium attracted much interest in recent years, due to a rich variety of characteristic features, attributed to the 4f-electrons [2]. In the case of Eu^{2+} ($4f^7$ configuration) the spin ($S = 7/2$), orbital ($L = 0$) and total ($J = 7/2$) angular momenta can be derived according to Hund's rule, yielding a high magnetic moment of $7.94 \mu_B/\text{Eu}^{2+}$, attributed only to the spins of the localized 4f-electrons [27]. In contrast, trivalent Eu^{3+} ($4f^6$) has a vanishing magnetic moment ($S = L = 3$, $J = 0$) in the ground state. Furthermore, depending on the valence state strongly different ionic radii occur, whereby the Eu^{2+} ion is about 20% bigger than Eu^{3+} , depending on the coordination number [14]. The Eu valence in intermetallic compounds thus depends on the local environment of the Eu-ions, as well as on the number and kind of nearest neighbors. As discussed by Doniach [15], the competition between the Ruderman-Kittel-Kasuya-Yosida (RKKY) interaction and the Kondo-effect suggests a generic p-T-phase diagram, which is greatly influenced by the tunable magnetic exchange interaction parameter J_{cf} between the conduction and 4f electrons. Interestingly, for Eu both valence states can be rather close in energy, leading to a variety of competing phenomena such as ferro-/antiferromagnetic ordering, Kondo-effect or valence crossover [2]. In the prototypical ternary compound EuPd_2Si_2 the valence-fluctuation is known to be accompanied by a large and abrupt reduction ($\sim 2\%$) of the tetragonal a-lattice parameter [1], implying a substantial interconnection between lattice and electronic degrees of freedom [5]. In particular, a valence transition from $\text{Eu}^{2+} \rightarrow \text{Eu}^{3+}$ may be tuned by temperature [1], high magnetic fields [34], hydrostatic [3] or chemical pressure due to, e.g., isoelectronic substitution of palladium by platinum in $\text{Eu}(\text{Pd}_{2-x}\text{Pt}_x)\text{Si}_2$ [4]. Recently, we have shown that it is possible to suppress the valence transition in epitaxial and highly crystalline $\text{EuPd}_2\text{Si}_2(001)/\text{MgO}(001)$ thin films due to the particularly strong coupling between the electronic fluctuations and the lattice degrees of freedom via a mechanical clamping effect to the stiff MgO substrate [12]. Poly- and single crystals of both binary compounds, EuPd_2 and EuPd_3 , show stable divalent and trivalent europium valencies down to lowest temperatures, respectively,

*Corresponding author. E-mail: koelsch@physik.uni-frankfurt.de

as explored, e.g., by Mössbauer [27, 22] or nuclear magnetic resonance (NMR) [28] spectroscopic studies. In the case of EuPd_2 , ferromagnetic ordering of Eu is observed below ~ 80 K [22] and the Curie temperature can be raised linearly by the application of hydrostatic pressure [18]. However, even in pressures up to 8 GPa the europium remains divalent in EuPd_2 . Previous NMR studies on EuPd_2 polycrystals revealed, that magnetic ordering is promoted by indirect RKKY exchange interaction through polarization of the $6s^2$ conduction electrons, donated from Eu [29].

In contradistinction, poly-[22] and single[19] crystal studies of EuPd_3 confirm a nonmagnetic ground state. Due to the thermal occupation of close-lying excited states of Eu^{3+} a weak and nearly temperature-independent Van Vleck susceptibility is experimentally observed in EuPd_3 with the trivalent Eu-state [20]. As possible reason for a small upturn of resistivity upon cooling below 10 K in EuPd_3 single crystals, exhibiting a slight excess of $\sim 0.1\%$ divalent Eu, Kondo-like behavior due to magnetic impurities was suggested [19]. As evident from previous photoemission studies of annealed europium films on palladium single crystals, most europium-palladium compounds contain some divalent Eu in the outermost layers independent of temperature [24, 25], indicating different properties at the surface as compared to the bulk [6, 26]. Unfortunately, strong interdiffusion effects even at liquid nitrogen temperatures inhibit the investigation of stoichiometric and epitaxial europium-palladium films if a palladium substrate is chosen [25]. Concerning epitaxial europium-palladium thin films we know of only one report, in which the codeposition of ultra thin films of EuPd_3 (< 4 nm) is investigated on $\text{MgO}(001)$ substrates and $\text{Fe}(001)$ templates by electron diffraction, photoelectron spectroscopy and ferromagnetic resonance experiments [13]. The authors conclude the growth mode on 600°C annealed $\text{MgO}(001)$ to be of the Vollmer-Weber type based on electron diffraction in-plane studies, where at first random in-plane (111)-textured islands coalesce and finally turn into a $\text{EuPd}_3(001)$ -film. This growth mode is supported by the similarity between fcc Pd and sc EuPd_3 (replacing palladium atoms in the corners of the fcc Pd unit cell by europium atoms yields the AuCu_3 structure of EuPd_3), whereby Pd grows island-like on $\text{MgO}(001)$ [35]. As evidenced from angle-resolved X-ray photoelectron spectroscopy experiments only a small fraction of Eu is divalent at room temperature [13]. To our knowledge, up to now no epitaxial thin film specific report regarding EuPd_2 on non-palladium substrates has been published, which leaves several questions unanswered. Furthermore, due to experimental difficulties for many RE-based compounds synthesis of phase-pure epitaxial thin films has not yet been achieved successfully [7]. In this study we report experimental results concerning the growth of epitaxial EuPd_3 and EuPd_2 thin films (thickness ~ 50 nm), as well as their structural and temperature-dependent magnetotransport properties.

2 Experimental details

Epitaxially grown thin films were prepared on $\text{MgO}(001)$ substrates using molecular beam epitaxy (MBE) in an ultra-high vacuum chamber described elsewhere [12]. During growth, the absolute pressure in the chamber did not exceed 5×10^{-9} mbar and was composed mainly ($\sim 90\%$) of hydrogen, due to the gas release from the heated europium source. Residual gas analysis was performed with a quadrupole mass spectrometer from Pfeiffer Balzers (model QMA120A). According to the results from our former epitaxial growth study on MgO substrates [12], no chemical cleaning of the substrate was performed in order to reduce possible growth-disturbing hydroxylation [9] and subsequent attack of the surface [8]. Instead, the substrates were degassed at 450°C for one hour and thermally cleaned at elevated temperature prior to growth as described below. For the deposition of Pd an electron beam evaporator was used, whose material flux was feedback-controlled by a water-cooled quartz crystal microbalance. Eu was sublimated from a pyrolytic boron nitride (PBN) crucible inside an effusion cell at a temperature between 440 - 470°C , with a stability better than 0.1°C . It is important to note that the substrate temperature during codeposition was held constant at 450°C and is comparable to the sublimation temperature of europium. Significant desorption may therefore take place at the surface and will influence the thin film growth, as discussed below. After codeposition the samples were allowed to cool to room temperature before an amorphous Si capping layer with a typical thickness of 5 nm was deposited using another electron beam evaporator to prevent further oxidation due to the highly reactive nature of europium. Before and after growth the surface crystallinity was inspected via reflection high-energy electron diffraction (RHEED) with a 15 keV electron source. No signs of crystallinity could be observed via RHEED after the deposition of the silicon film. Scanning electron microscopy (SEM) images were acquired ex-situ in a FEI Nova NanoLab 600 to study the surface morphology. Structural characterization via symmetric and asymmetric X-ray diffraction (XRD) was done with a Bruker D8 Discover high-resolution diffractometer using $\text{Cu}_{K,\alpha}$ radiation with a parallelized primary beam and a diffracted-side monochromator in air. For analysis of the X-ray scans, revealing high and low angle oscillations, Bruker's DiffracPlus Leptos Software was used.

3 Results and discussion

3.1 $\text{EuPd}_3/\text{MgO}(001)$

3.1.1 Growth mode and structural properties

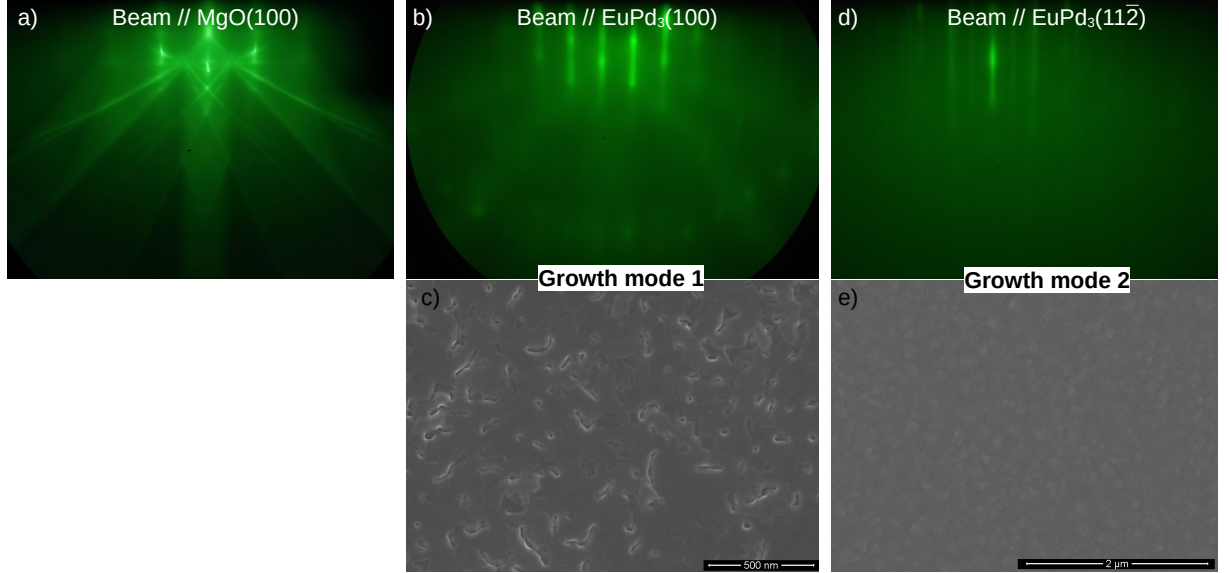


Figure 1: a) RHEED image of the pure $\text{MgO}(001)$ substrate with beam along the $[100]$ direction, directly before codeposition. b) and d) RHEED images after thin film deposition and before Si capping, grown in mode 1 and mode 2 without any change of sample position. c) and e) corresponding SEM images of the EuPd_3 films including the Si capping layer. The scale bar corresponds to 500 nm and 2 μm , respectively.

In comparison to the cubic lattice parameter of fcc MgO $a = 4.212 \text{ \AA}$ [10], EuPd_3 has a simple cubic structure with $a = 4.09 \text{ \AA}$ [16]. Calculation of the lattice mismatch at room temperature thus yields about -3%, i.e. a small tensile strain for an epitaxial EuPd_3 film may be expected. As reported before, low temperature annealing of the MgO substrate just before codeposition leads to the first growth mode of EuPd_3 on $\text{MgO}(001)$ [13], here called mode 1. Upon rotation of the pure MgO substrate after annealing at 600°C around the surface normal, RHEED azimuthal scans show a fourfold symmetry, see Fig. 1 a). Subsequent to the codeposition of the EuPd_3 thin film the same fourfold symmetry is observed, see Fig. 1 b). Without any sample rotation the RHEED pattern of the thin film shows equidistant long streaks and reflexes also in the first order Laue circle, indicative of high structural in-plane order. Comparison of the directions for the main symmetry axes from the substrate and the thin film implies a parallel alignment of their crystallographic a -axes and a simple cube-on-cube growth model can be stated. Furthermore, broad Kikuchi bands are clearly visible, pointing to a laterally well-ordered crystalline film on the length scale of several hundred nanometers. SEM (Fig. 1 c) images of the Si-capped thin films reveal a rather smooth and flat topography with some valleys and holes on a lateral scale of about 50-200 nm.

Choosing a substrate annealing temperature of 1000°C for one hour leads to another growth mode, herein called mode 2. Such prepared MgO surfaces show nearly the same RHEED patterns as before. Direct observation of the RHEED pattern after thin film growth reveals however less contrast and only very long streaks near the zeroth order Laue circle. In addition, without any sample rotation weak lines between stronger main lines appear, see Fig. 1 d). Furthermore, no Kikuchi bands or lines develop, implying less in-plane order in growth mode 2. Interestingly, rotation of the sample yields the same pattern every 60° . SEM images (see Fig. 1 e) only exhibit weak contrast, without any visible holes or valleys. Instead, some small triangular facets can be observed on close inspection, indicating a very flat thin film with strongly coalesced (111) -oriented islands.

For both growth modes Kiessig fringes arise from a relatively smooth interface and surface, which are visible in symmetric low angle X-ray reflectometry (XRR) scans (Fig. 2 a) up to $2\Theta = 3^\circ$. From this an average film thickness d of $39 \pm 1 \text{ nm}$ for EuPd_3 in mode 1 and $50 \pm 1 \text{ nm}$ for mode 2 is deduced,

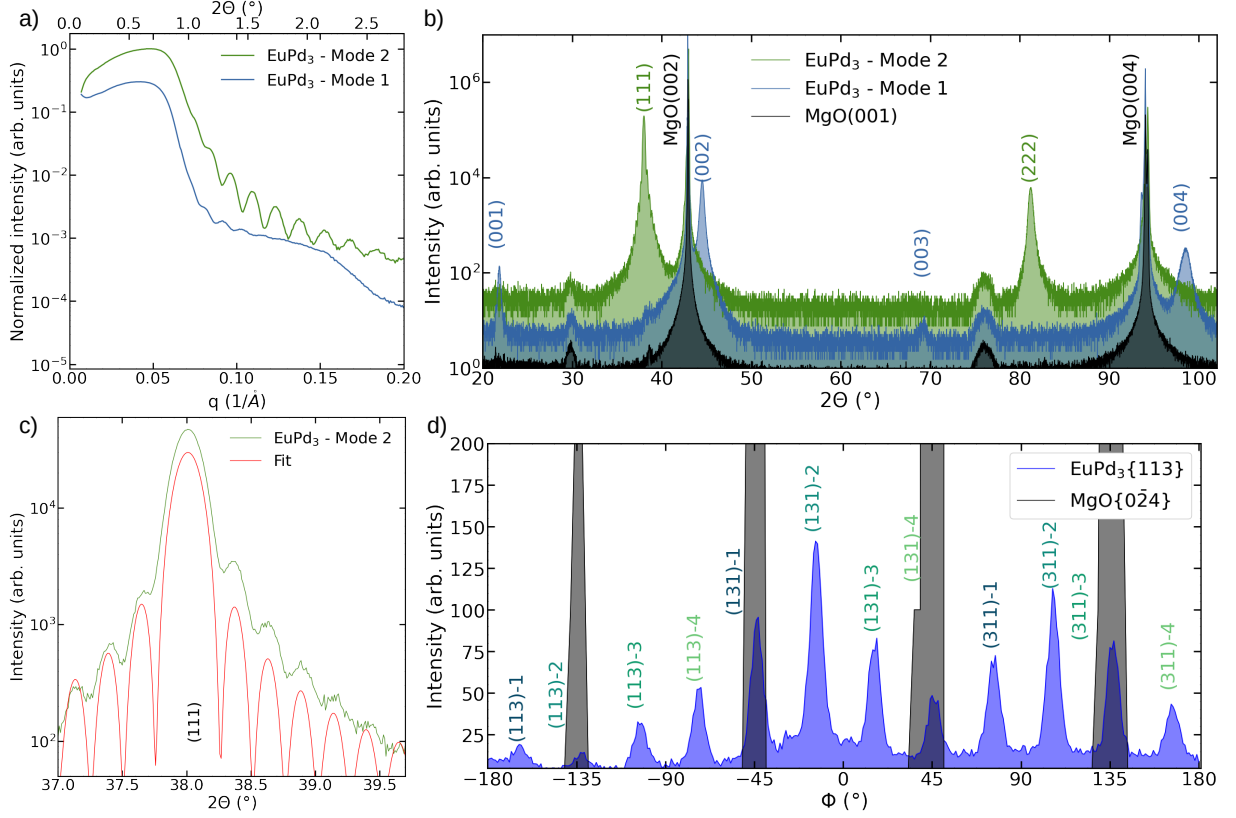


Figure 2: a) X-ray reflectometry scan of two EuPd_3 thin films, grown in mode 1 (blue) or 2 (green). Curves are offset for clarity. b) Wide angle symmetric scan of two different EuPd_3 thin films grown in mode 1 and 2, respectively. A scan of native $\text{MgO}(001)$ substrate is shown for reference. c) Magnification of a longitudinal symmetric X-ray diffractogram near the $\text{EuPd}_3(111)$ -reflex, grown in mode 2. Fit (red) of the Laue oscillations is included. d) Asymmetric XRD scan of the $\text{MgO}\{024\}$ - and $\text{EuPd}_3\{113\}$ -reflex families. See text for details.

respectively. For the second growth mode a slightly thicker film with longer codeposition time was chosen, which showed more oscillations, indicating less interfacial and surface roughness. The symmetric high angle X-ray diffraction scan (Fig. 2 c) reveals in mode 1 only (00ℓ) -reflexes of EuPd_3 with natural number ℓ appearing up to the 4th order, suggesting a well-ordered epitaxial thin film. In case of mode 2 only the $\text{EuPd}_3(111)$ - and $\text{EuPd}_3(222)$ -reflex occur with high intensity. Furthermore, Laue oscillations next to the $\text{EuPd}_3(111)$ -reflex (Fig. 2 b) indicate a high degree of structural order for the out-of-plane direction with a crystalline coherence length $L_c \approx 37$ nm. This suggests $\sim 95\%$ crystalline volume fraction in the out-of-plane direction with respect to the total layer thickness of $d = 39$ nm, which was obtained by analysis of the Kiessig fringes. Around 76° a broad and small reflex is visible for all films and the pure MgO substrate, which appears due to scattering from the sample holder. In both modes no crystalline impurity phase is detected, implying phase-pure epitaxial growth of either $\text{EuPd}_3(100)$ or $\text{EuPd}_3(111)$ on $\text{MgO}(001)$, depending solely on the annealing temperature of the substrate and therefore the surface conditions prior to growth. Additional asymmetric X-ray diffractograms (not shown) confirm the epitaxial relationship for the first growth mode as deduced from RHEED to be:

$$(1): \text{MgO}\{100\} \parallel \text{EuPd}_3\{100\} \ \& \ \text{MgO}\langle 001 \rangle \parallel \text{EuPd}_3\langle 001 \rangle$$

In the high temperature annealing case (growth mode 2) instead an asymmetric XRD ϕ -Scan (Fig. 2 d) of the $\text{EuPd}_3\{113\}$ -reflex family reveals four equivalent rotational in-plane domains (labelled by different colors and numbers 1-4), which form the epitaxial relationship according to:

$$(2): \text{MgO}\{100\} \parallel \text{EuPd}_3\{111\} \ \& \ \text{MgO}\langle 010 \rangle \parallel \text{EuPd}_3\langle 11\bar{2} \rangle$$

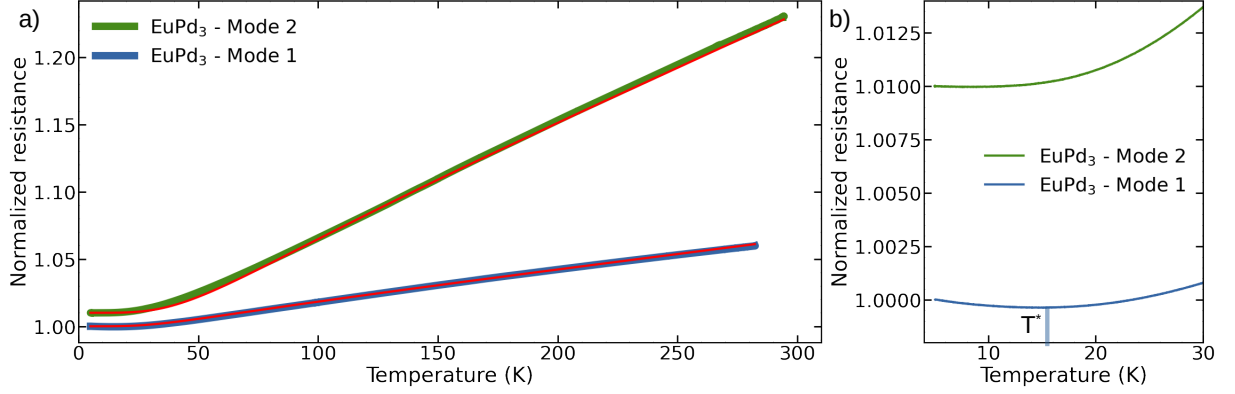


Figure 3: a) Resistance of the same two EuPd_3 films as before, normalized to the value at 5 K. The upper curve is shifted for clarity. Included are fits (red) according to the Bloch-Grüneisen model. b) Detailed view of the low temperature region, revealing a resistance minimum at T^* around 15 K for the first growth mode. See text for details.

3.1.2 Magnetotransport properties

Patterning of thin films utilizing UV-photolithography and low-energy (<1000 eV) Ar-ion sputtering were done to fabricate 6-contact Hall bar structures with a cross-area of $30 \times 100 \mu\text{m}^2$. Low temperature magnetotransport measurements were performed inside a helium flow cryostat via a variable temperature insert between 3 K and 300 K in a magnetic field up to 5 T. The measurements were done at a constant current of $100 \mu\text{A}$, leading to current densities smaller than $1 \cdot 10^8 \text{ A/m}^2$. For both growth modes, a simple metallic behavior below room temperature is visible in the normalized resistance, see Fig. 3 a). Interestingly, the calculated resistivity and residual resistivity ratios (RRR) values vary significantly, despite the quite similar thicknesses. For the film grown in mode 1 $\rho_1(T = 4 \text{ K}) = 130 \mu\Omega\text{cm}$ and $\text{RRR}_1 \sim 1.06$, whereas for growth mode 2 a much smaller resistivity of $\rho_2(4 \text{ K}) = 37 \mu\Omega\text{cm}$ and $\text{RRR}_2 = 1.22$ is calculated. Both properties thus reflect the higher structural order or crystallinity, which may be obtained by high temperature annealing of the substrate. Roughly above 50 K the resistance scales for both variants linearly with respect to temperature and becomes nearly constant below about 20 K. Furthermore, a resistivity minimum develops for the film in the first growth mode at a temperature of $T^* \approx 15 \text{ K}$, see Fig. 3 b). A similar resistance minimum is observed in well-ordered single crystals, with $\rho_0 = 2.4 \mu\Omega\text{cm}$ and $\text{RRR} = 3.1$, which also show de Haas-van Alphen oscillations [19]. As there seems to be no contribution of higher J-multiplets of EuPd_3 to the resistivity, a simple Bloch-Grüneisen model due to phonon scattering at elevated temperatures seems appropriate. In the bulk case this leads to a Debye temperature of $\Theta_D \sim 230 \text{ K}$ [19]. Evaluating this simple model to films of both growth modes shows good agreement, as can be seen from the concordance with the fits (red lines) in Fig. 3 a). Here Debye temperatures of 189 K (mode 1) and 256 K (mode 2) are obtained, which are as well comparable with $\Theta_D \sim 280 \text{ K}$ of pure palladium [17]. In the case of lower crystallinity films in mode 1, the deviation from single crystal behavior is more pronounced, which can be seen, e.g., in ρ_0 , RRR and Θ_D . Complementary measurements of the Hall effect (HE), i.e., the Hall resistance, always reveal a negative linear Hall coefficient with applied magnetic field in the out-of-plane direction for temperatures below 300 K (not shown). Assuming a single-band model for the charge carriers thus leads to a nearly constant, electron-like charge carrier density of $\sim 6 \cdot 10^{28} \text{ m}^{-3}$. Furthermore, measurements of the longitudinal magnetoresistance ($\text{MR} = [\rho(B) - \rho(B = 0)] / \rho(B = 0)$) at low temperatures ($< 10 \text{ K}$) show a negligible but positive effect, i.e., a marginally larger resistivity of well below +0.1% at 5 T, as compared to the zero field value for films of both growth modes (not shown).

3.2 $\text{EuPd}_2/\text{MgO}(001)$

3.2.1 Growth and structural properties

Since EuPd_2 crystallizes in the cubic Laves phase C15 with lattice constant $a = 7.763 \text{ \AA}$ [21], a simple cube-on-cube model as (for EuPd_3) may not be expected due to the high misfit of $\sim 7\%$ with $\text{MgO}(001)$. No previous study regarding the epitaxial growth of EuPd_2 via codeposition exists, so the deposition parameters from the successful EuPd_3 growth on $\text{MgO}(001)$, as stated above, were used first. In con-

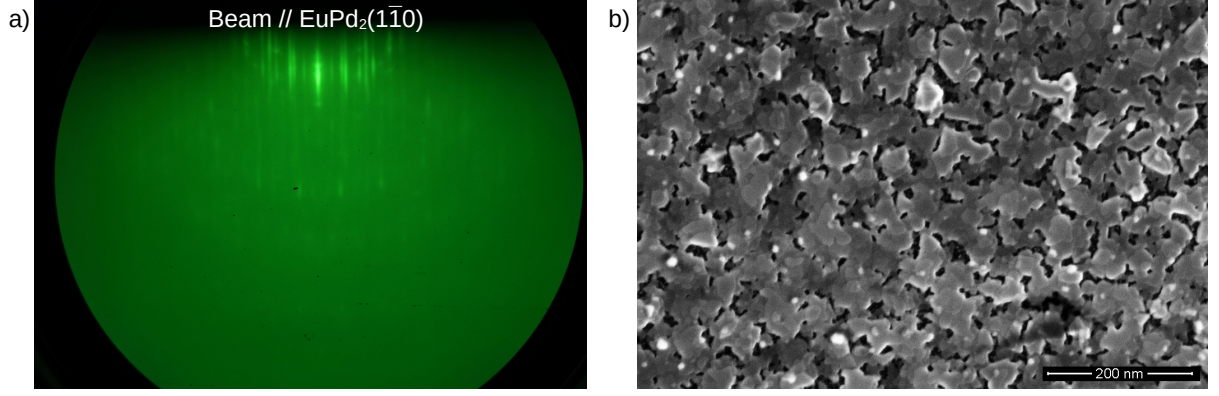


Figure 4: a) RHEED image subsequent to thin film deposition after rotation of the sample to a main symmetry direction of the pattern. b) Corresponding SEM image of the EuPd_2 film including the Si capping layer. The scale bar corresponds to 200 nm.

tradistinction to the behavior of EuPd_3 no change of the out-of-plane growth direction was observed, through changing the MgO substrate annealing temperature. Instead, more crystal orientations evolve at lower substrate annealing temperatures around 600 °C, i.e., more intense (100)-, (110)- and (311)-crystal facettes become visible in the high-angle symmetric XRD scans (not shown). Furthermore, a lower crystallinity manifests itself in more diffuse RHEED patterns with additional weak dots, indicative of small islands and a very rough surface. Best conditions for EuPd_2 growth were found to be an annealing temperature of 1000 °C for one hour, a substrate temperature of 450 °C during codeposition and an effective slow growth rate around 0.1 Å/s with stoichiometrically matched Eu and Pd fluxes. RHEED azimuthal in-plane scans of a thus prepared thin film exhibit a sixfold symmetry upon rotation with many streaks, including some satellites and also higher order Laue circles (Fig. 4 a). Together with the SEM image (Fig. 4 b), revealing triangular formed and weakly coalesced islands, we conclude a pronounced island-like growth behavior of EuPd_2 with two in-plane domain variants.

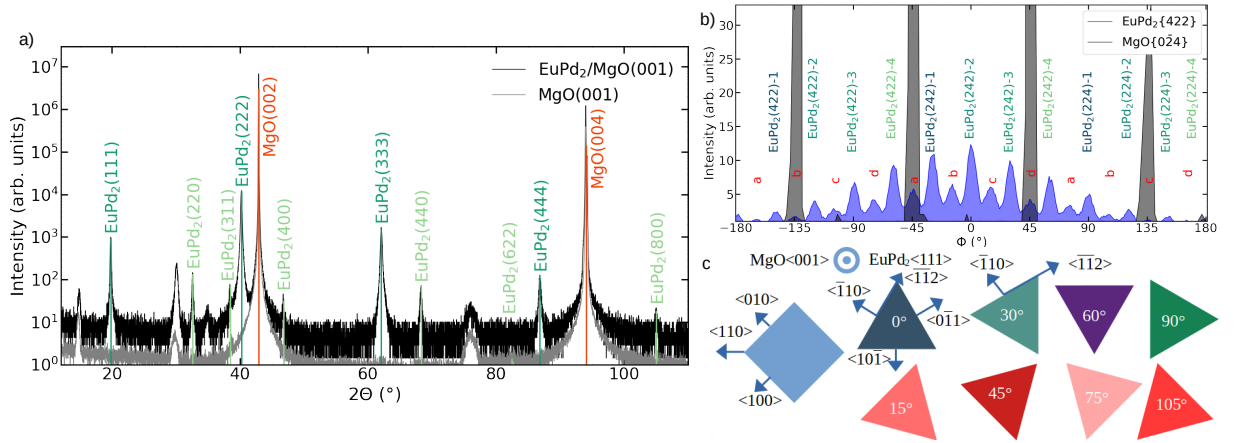


Figure 5: a) Longitudinal symmetric X-ray diffractogram of an epitaxial EuPd_2 thin film and a pure MgO(001) substrate. b) ϕ -scan around sample normal of MgO{024}- and EuPd_2 {422}-reflexes in asymmetric geometry. The reflex families for the main in-plane domains are indicated in blueish/greenish colors. Additionally, four minor domains are highlighted by a)-d) in reddish colors. c) Top view sketch of the orientation variants for the main domains (0°, 30°, 60°, 90°) and the minor domains (15°, 45°, 75°, 105°) with respect to the MgO square lattice (light blue) with crystallographic directions as indicated by arrows.

Regarding the symmetric high-angle XRD scan (Fig. 5 a) a strong $\langle 111 \rangle$ -out-of-plane orientation for EuPd_2 is clearly visible, thus supporting the former findings from the RHEED experiments. Although some minor other crystal facets are visible within a logarithmic scale of the intensity, the amount of crystallographic disorder is small. Additionally, no other crystalline chemical phase appears, as, e.g., EuPd_2Si_2 may be expected upon intermixing with the silicon capping layer. Besides the $\text{EuPd}_2(111)$ -reflex

small shoulders as Laue oscillations arise, yielding a coherent thickness of $L_c \approx 20$ nm. Careful inspection of small angle X-ray scans (not shown) do not reveal any Kiessig fringes, pointing to a non-uniform or rough surface, already seen in the SEM images. Rocking curve measurements of, e.g., the $\text{EuPd}_2(222)$ reflex exhibit a full width at half maximum (FWHM) of 0.34° , thus revealing only little mosaic spread and a strong out-of-plane alignment. Further ϕ -scans around the sample's surface normal in asymmetric reflection geometry of the $\text{MgO}\{024\}$ - and $\text{EuPd}_2\{422\}$ -reflexes show regularly spaced peaks 90° and 30° apart, respectively. The intensity of all reflexes varies with ϕ , due to a small sample tilt offset $\sim 0.01^\circ$ with respect to the diffractometer's ϕ -circle. This offset has no effect on the conclusions regarding the in-plane crystallographic order. For EuPd_2 different main in-plane orientations, labelled with varying colors and heights in Fig. 5 b), are clearly visible and correspond to the four upper orientation models of $\text{EuPd}_2(111)$ depicted in the sketch in Fig. 5 c). Furthermore, some small equidistant peaks (labelled with a to d) are visible between those major EuPd_2 reflexes, indicating additional in-plane variants, which are sketched below the main domain variants in reddish colors in Fig. 5 c). For the main domains, $\text{EuPd}_2(10\bar{1})$ aligns parallel with $\text{MgO}\{110\}$, whereas in the case of the minor domains we find $\text{EuPd}_2\{10\bar{1}\} \parallel \text{MgO}\{010\}$, leading to an epitaxial relationship for the main in-plane rotational domains:

$$\text{MgO}\{100\} \parallel \text{EuPd}_2\{111\} \ \& \ \text{MgO}\langle 110 \rangle \parallel \text{EuPd}_2\langle 10\bar{1} \rangle$$

And for the minor in-plane domains:

$$\text{MgO}\{100\} \parallel \text{EuPd}_2\{111\} \ \& \ \text{MgO}\langle 100 \rangle \parallel \text{EuPd}_2\langle 10\bar{1} \rangle$$

3.2.2 Magnetotransport properties

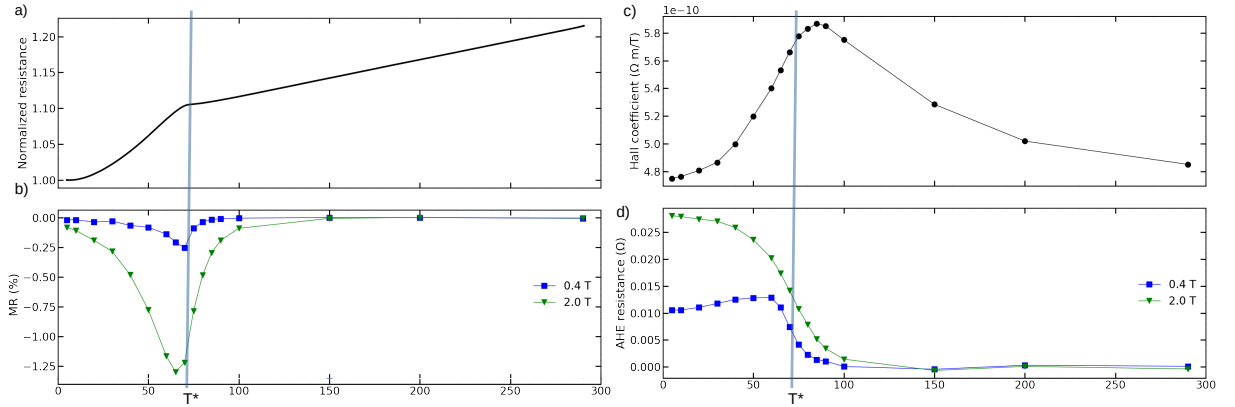


Figure 6: a) Temperature dependence of the electrical 4-wire resistance of the EuPd_2 thin film normalized to the value at 5 K. b) Transverse magnetoresistance $\text{MR}(B) = (\rho(T, B) - \rho(T, B = 0)) / \rho(T, B = 0)$ with magnetic field oriented out-of-plane. c) Normal Hall coefficient R_0 as obtained by a linear fit to the high field data above 2 T at constant temperatures. d) Anomalous Hall resistance for two different magnetic fields at constant temperatures, as determined after subtracting the field dependent normal Hall contribution. See text for details.

The temperature dependence of the resistivity, shown in Fig. 6 a), reveals a metallic behavior of the lithographically patterned EuPd_2 thin film, as expected from single crystal data. Above ~ 90 K the resistivity scales linearly with temperature, which is indicative of electron-phonon scattering. Around 72 ± 1 K a kink is visible, pointing to the onset of magnetic ordering in zero applied field. The residual resistivity ratio (RRR) between 280 K and 3 K amounts to only ~ 1.2 , which is nearly equal to the values obtained for highly crystalline EuPd_3 shown above. Using the coherent thickness of 20 nm, as obtained by analyzing the Laue oscillations, for the calculation of the resistivity for $T \rightarrow 0$ gives a high value around $\rho_0 \approx 311 \mu\Omega\text{cm}$. Below ~ 72 K the resistivity follows $\rho(T) = \rho_0 + AT^2$, with coefficient $A = 8.12 \cdot 10^{-3} \mu\Omega\text{cm}/\text{K}^2$. The T^2 behavior can be attributed to arising electron-magnon scattering in the magnetically ordered phase [18]. Due to the weakly connected nature of the islands, the actual in-island resistivity and therefore ρ_0 might be much smaller. In contrast, EuPd_2 single crystals exhibit a higher RRR around 19 with a residual resistivity of $\rho_0 \approx 1.5 \mu\Omega\text{cm}$ for current direction parallel to the a-axis [18]. In consequence, the electrical transport in epitaxial thin films of EuPd_2 is strongly influenced by grain boundary scattering between (weakly) coalesced islands with possible different in-plane orientation.

Reflecting the distribution of the eight domain variants as obtained by asymmetric XRD scans, a strong increase in resistivity and decrease of RRR is to be expected.

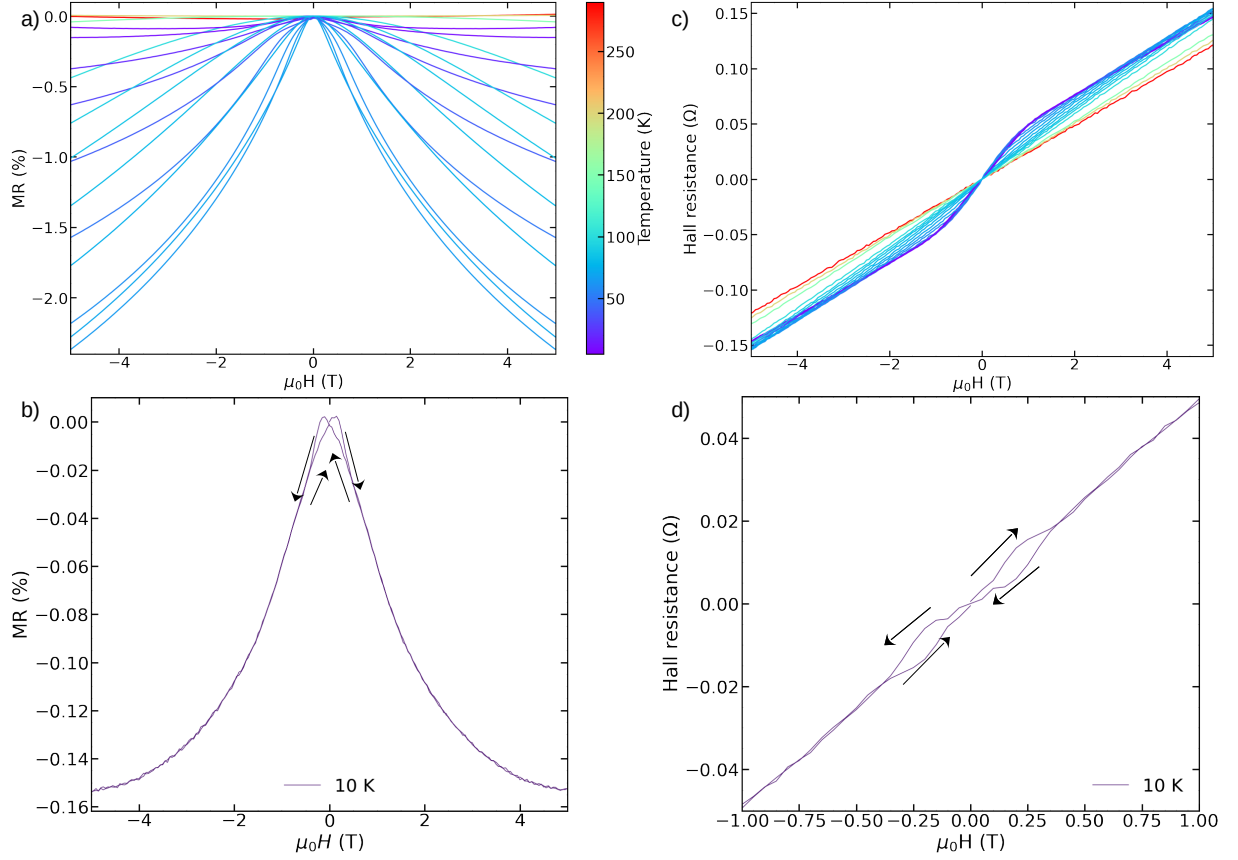


Figure 7: Magnetic field dependence of MR (a) and Hall resistance (c) at constant temperatures, as indicated by the colorbar. MR (b) and Hall resistance (d) at 10 K as a function of applied magnetic field $\mu_0 H$, respectively. Arrows indicate sweep direction of the magnetic field. See text for details.

To further investigate the magnetic properties, longitudinal magnetoresistance and Hall effect measurements were performed in an applied field perpendicular to the surface up to 5 T. As is evident from Fig. 6 b) a small negative magnetoresistance due to decreasing scattering from magnetic fluctuations or magnetic domain boundaries below about 70 K is observed. At higher temperatures, i. e., above 100 K, no significant magnetoresistance effect is observed. Interestingly, the temperature dependence of the magnetoresistance $MR(T, B = 0.4 \text{ T})$, reveals a global minimum at the same magnetic ordering temperature T^* seen in the zero-field resistivity curve (Fig. 6 a). Above T^* the MR evolves as downward opened parabola, whose curvature decreases with increasing temperature (Fig. 7 a). In contrast, below T^* the shape of MR exhibits a change in curvature in fields above $\sim 1.5 \text{ T}$. Furthermore, in fields below 0.4 T hysteresis effects appear upon sweeping the magnetic field, which can be clearly seen in Fig. 7 b).

For ferromagnetic materials the Hall resistance or the transverse resistivity ρ_{xy} may be divided into the ordinary or normal Hall effect (NHE) $\rho_{xy}^{NHE} \propto B$ and the anomalous Hall effect (AHE) $\rho_{xy}^{AHE} \propto M$ with proportionality constants R_0 and R_S , respectively.

$$\rho_{xy} = \rho_{xy}^{NHE}(B, T) + \rho_{xy}^{AHE}(M, T) = R_0(T)B + R_S(T)\mu_0 M(T)$$

Due to the saturation behavior of the anomalous Hall effect, corresponding to a saturation of the magnetization, the normal Hall effect contribution can be obtained by a linear fit to the high field data (here above 2 T, see Fig. 7 c). From the coefficient of the linear slope, we obtain the normal Hall coefficient $R_0(T)$, whose temperature dependence is shown in Fig. 6 c). Again, a broad maximum near T^* evolves, although the effect of temperature on R_0 is small. Calculation of the charge carrier density yields around $1 \cdot 10^{28} \text{ m}^{-3}$, whereby the carriers behave hole-like in a single-band mode. It should be noted that a hysteretic behavior of ρ_{xy} is observed, below the magnetic ordering temperature and $\mu_0 H \lesssim 0.4 \text{ T}$ (Fig. 7 d).

Subtraction of the normal Hall contribution leaves the anomalous Hall resistance, whose temperature dependence shows the steepest decrease near T^* for different applied fields (Fig. 6 d). As the magnitude of the anomalous Hall effect increases with decreasing temperature and shows both saturation and hysteresis effects as a function of magnetic field, a ferromagnetic ground state is likely.

4 Conclusion

In summary, we demonstrated the epitaxial growth of EuPd_2 and EuPd_3 on $\text{Mg}(001)$ substrates using molecular beam epitaxy, with a typical lateral island size of the order of several hundred nm. For all thin films investigated, a relaxed growth takes place, such that the cubic a-lattice parameters are equal to their bulk crystal values. Depending on the substrate annealing temperature and therefore the surface condition of MgO , two different epitaxial relationships are observed for EuPd_3 thin films. For annealing temperatures of 600°C a simple cube-on-cube relationship is established, showing a defect- or impurity-induced resistance minimum around 15 K, which is also known from single crystal studies and was attributed to a Kondo effect [19]. In the high temperature annealing case, a $\text{EuPd}_3(111)$ orientation is obtained, where the film is nearly fully coherent (about 95%) in the out-of-plane direction. According to RHEED azimuthal scans multiple in-plane domains form, which is also known, e.g., in the simple system $\text{Pt}/\text{MgO}(001)$ [11]. In consequence of the higher structural order in mode 2, the residual resistivity is smaller, the RRR is larger and the resistance minimum disappears completely. Thin films of EuPd_3 thus are less prone to contamination with respect to magnetic impurities as, e.g., potentially Eu^{2+} in EuPd_3 single crystals. This might be analogous to the case of EuO thin films, whereby reevaporation of unreacted Eu-metal occurs at sufficiently large substrate temperatures on inert YAlO_3 [30] or yttria-stabilized zirconia [31] substrates, thus avoiding off-stoichiometry or build up of Eu metal clusters under optimum growth conditions. An XPS study on the influence of different cleaning methods on the surface conditions on $\text{MgO}(001)$ substrates revealed that after vacuum annealing at 700°C for 2 h without any wet-chemical cleaning, still a small amount of $\text{Mg}(\text{OH})_2$ remains at the surface [9]. The authors claim that further annealing above 900°C is necessary to desorb this surface-bound layer, while at the same time calcium segregation to the surface will slowly take place. In consequence, the different surface chemistry due to the substrate annealing in the investigated growth modes here, might be responsible for the pronounced change of both, the epitaxial thin film relationship and the amount of crystalline or structural order. Even after many years of investigations, the optimum substrate cleaning method for MgO remains under discussion and has to be carefully considered with respect to the growing thin film [9].

In addition, for the first time EuPd_2 thin films could be grown with an epitaxial relationship possessing four main in-plane domains, namely $\text{MgO}\{100\}||\text{EuPd}_2\{111\}$ and $\text{MgO}\langle 110 \rangle || \text{EuPd}_2[10\bar{1}]$, as deduced by room temperature RHEED and symmetric and asymmetric XRD experiments. Besides these, a minority of the in-plane domains exhibits another crystallographic orientation according to $\text{MgO}\{100\}||\text{EuPd}_2\{111\}$ and $\text{MgO}\langle 100 \rangle || \text{EuPd}_2[10\bar{1}]$, which are thus rotated by 15° with respect to the main domains around the growth direction. For EuPd_2 surface chemistry seems to play a minor role with respect to the epitaxy, although higher annealing temperatures promote a better film crystallinity. SEM images indicate an island-like growth mode for $\text{EuPd}_2(111)$ on $\text{MgO}(001)$, which occurs likewise, e.g., for Pd on MgO [35] or $\text{EuPd}_2\text{Si}_2/\text{MgO}(001)$ [12], suggesting a high interfacial energy and a strong tendency for dewetting from the MgO substrate. Magnetotransport measurements reveal a magnetic phase transition around 72 K, which corresponds well to the ferromagnetic ordering in single [18] and polycrystals [28]. In combination with the Hall effect investigations, a ferromagnetic ground state of the EuPd_2 seems most likely.

To reduce the amount of crystalline in-plane disorder due to rotational domain formation, as seen, e.g., in the resistivity or in RRR, our future studies will focus on the growth of both compounds with the (111) out-of-plane orientation on symmetry-adopted substrates. Research along these lines is under way.

5 Acknowledgment

Funded by the Deutsche Forschungsgemeinschaft (DFG, German Research Foundation) - TRR288 - 422213477 (project A04).

References

- [1] E. V. Sampathkumaran, L. C. Gupta, R. Vijayaraghavan, K. V. Gopalakrishnan, R. G. Pillay, and H. G. Devare, A new and unique Eu-based mixed valence system: EuPd_2Si_2 . *Journal of Physics C: Solid State Physics* (1981), 14(9):L237-L241.
- [2] Y. Ōnuki, A. Nakamura, F. Honda, D. Aoki, T. Tekeuchi, M. Nakashima, Y. Amako, H. Harima, K. Matsubayashi, Y. Uwatoko, S. Kayama, T. Kagayama, K. Shimizu, S. Esakki Muthu, D. Braithwaite, B. Salce, H. Shiba, T. Yara, Y. Ashitomi, H. Akamine, K. Tomori, M. Hedo, and T. Nakama, Divalent, trivalent, and heavy fermion states in Eu compounds, *Philosophical Magazine* (2017), 97(36):3399–3414.
- [3] D. M. Adams, A. E. Heath, H. Jhans, A. Norman, and S. Leonard, The effect of high pressure upon the valence transition in EuPd_2Si_2 , *Journal of Physics: Condensed Matter* (1991), 3(29):5465–5468.
- [4] A. Mitsuda, H. Wada, M. Shiga, H. Aruga Katori, and T. Goto, Field-induced valence transition of $\text{Eu}(\text{Pd}_{1-x}\text{Pt}_x)_2\text{Si}_2$, *Physical Review B* (1997), 55(18):12474–12479.
- [5] K. Kliemt, M. Peters, I. Reiser, M. Ocker, F. Walther, D.-M. Tran, E. Cho, M. Merz, A. A. Haghighirad, D. C. Hezel, F. Ritter, and C. Krellner, Influence of the Pd-Si ratio on the Valence Transition in EuPd_2Si_2 Single Crystals, *Crystal Growth & Design* (2022).
- [6] G. K. Wertheim, E. V. Sampathkumaran, C. Laubschat, and G. Kaindl, Final-state effects in the x-ray photoemission spectrum of EuPd_2Si_2 , *Physical Review B* (1985), 31(10):6836–6839.
- [7] S. Chatterjee. Heavy fermion thin films: progress and prospects, *Electronic Structure* (2021), 3(4):043001.
- [8] C. Duriez, C. Chapon, C. R. Henry, and J. M. Rickard, Structural characterization of $\text{MgO}(100)$ surfaces, *Surface Science* (1990), 230(1-3), 123-136.
- [9] Le Febvrier, J. Jensen, and P. Eklund, Wet-cleaning of $\text{MgO}(001)$: Modification of surface chemistry and effects on thin film growth investigated by x-ray photoelectron spectroscopy and time-of-flight secondary ion mass spectroscopy, *Journal of Vacuum Science & Technology A: Vacuum, Surfaces, and Films* (2017), 35(2), 021407.
- [10] D. K. Smith and H. R. Leider, Low-temperature thermal expansion of LiH , MgO and CaO . *Journal of Applied Crystallography* (1968), 1(4):246–249.
- [11] C. Gatel, P. Baules, and E. Snoeck, Morphology of Pt islands grown on $\text{MgO}(001)$, *Journal of crystal growth* (2003), 252(1-3), 424-432.
- [12] S. Kölsch, A. Schuck, M. Huth, O. Fedchenko, D. Vasilyev, S. Chernov, O. Tkach, H.-J. Elmers, G. Schönhense, C. Schlüter, T. R. F. Peixoto, A. Gloskowski, and C. Krellner, Clamping effect on temperature-induced valence transition in epitaxial EuPd_2Si_2 thin films grown on $\text{MgO}(001)$, *Physical Review Materials* (2022), 6(11), 115003.
- [13] P. Maślankiewicz, Z. Celinski, and J. Szade, Europium-palladium intermetallic thin layers, *Journal of Physics: Condensed Matter* (2008), 20(31).
- [14] R. D. Shannon, Revised effective ionic radii and systematic studies of interatomic distances in halides and chalcogenides, *Acta crystallographica section A: crystal physics, diffraction, theoretical and general crystallography* (1976), 32(5), 751-767.
- [15] S. Doniach, Phase Diagram for the Kondo Lattice, In: R. D. Parks (eds) *Valence Instabilities and Related Narrow-Band Phenomena* (1977), Springer, Boston.
- [16] P. Villars and L. D. Calvert, *Pearson’s Handbook of Crystallographic Data for Intermetallic Phases* (1991), 2nd edition, vol. 4 Materials Park, OH: ASM International
- [17] R. A. Matula, Electrical resistivity of copper, gold, palladium, and silver, *Journal of Physical and Chemical Reference Data* (1979), 8(4), 1147-1298.

- [18] A. Nakamura, H. Akamine, Y. Ashitomi, F. Honda, D. Aoki, T. Takeuchi, K. Matsubayashi, Y. Uwamoto, Y. Tatetsu, T. Maehira, M. Hedo, T. Nakama, Y. & Ōnuki, Magnetic and Fermi Surface Properties of Ferromagnets EuPd_2 and EuPt_2 , *Journal of the Physical Society of Japan* (2016), 85(8), 084705.
- [19] T. Takeuchi, A. Nakamura, M. Hedo, T. Nakama, and Y. & Ōnuki, Contribution of J-multiplet levels to the physical properties of EuPd_3 with the trivalent electronic state, *Journal of the Physical Society of Japan* (2014), 83(11), 114001.
- [20] W. E. Gardner, J. Penfold, T. F. Smith, and I. R. Harris, The magnetic properties of rare earth-Pd₃ phases, *Journal of Physics F: Metal Physics* (1971), 2(1), 133.
- [21] I. R. Harris, and G. V. Raynor, Rare-earth intermediate phases: II. Phases formed with palladium, *Journal of the Less Common Metals* (1965), 9(4), 263-269.
- [22] I. R. Harris, G. Longworth, A study of the lattice spacings, magnetic susceptibilities and ^{151}Eu Mössbauer spectra of some palladium-europium alloys, *Journal of the Less Common Metals* (1971), 23(3), 281-292.
- [23] A. Iandelli, A. Palenzona, The europium-palladium system, *Journal of the Less Common Metals* (1974), 38(1), 1-7.
- [24] F. Bertran, T. Gourieux, G. Krill, M. Alnot, J. J. Ehrhardt, and W. Felsch, Growth of Eu on Pd(111): AES, photoemission and RHEED studies, *Surface Science Letters* (1991), 245(1-2), L163-L169.
- [25] F. Bertran, T. Gourieux, G. Krill, M. F. Ravet-Krill, M. Alnot, J. J. Ehrhardt, and W. Felsch, Growth of Eu on Pd(111) studied by x-ray and uv photoemission and crystallographic properties as determined by reflection-high-energy-electron-diffraction and x-ray-diffraction studies, *Physical Review B* (1992), 46(12), 7829.
- [26] F. Bertran, T. Gourieux, G. Krill, M. F. Ravet-Krill, M. Alnot, J. J. Ehrhardt, and W. Felsch, The Eu/Pd(111) interface: spectroscopic and structural studies, *Surface science* (1992), 269, 731-736.
- [27] H. H. Wickman, J. H. Wernick, R. C. Sherwood, and C. F. Wagner, Mössbauer and magnetic properties of several europium intermetallic compounds, *Bell Telephone Labs. (1967), Inc., Murray Hill, NJ.*
- [28] H. Kropp, E. Dormann, and K. H. J. Buschow, Electric field gradient in cubic intermetallic europium compounds with unstable europium valence, *Solid State Communications* (1979), 32(7), 507-510.
- [29] H. Kropp, W. Zipf, E. Dormann, and K. H. J. Buschow, Indirect exchange in intermetallic europium compounds, *Journal of Magnetism and Magnetic Materials* (1979), 13(1-2), 224-230.
- [30] R. W. Ulbricht, A. Schmehl, T. Heeg, J. Schubert, and D. G. Schlom, Adsorption-controlled growth of EuO by molecular-beam epitaxy, *Applied physics letters* (2008), 93(10), 102105.
- [31] S. G. Altendorf, A. Efimenko, V. Olliana, H. Kierspel, A. D. Rata, and L. H. Tjeng, Oxygen off-stoichiometry and phase separation in EuO thin films, *Physical Review B* (2011), 84(15), 155442.
- [32] K. Mimura, T. Uozumi, T. Ishizu, S. Motonami, H. Sato, Y. Utsumi, S. Ueda, A. Mitsuda, K. Shimada, Y. Taguchi, Y. Yamashita, H. Yoshikawa, H. Namatame, M. Taniguchi, and K. Kobayashi, Temperature-Induced Valence Transition of EuPd_2Si_2 Studied by Hard X-ray Photoelectron Spectroscopy, *Japanese Journal of Applied Physics* (2011), 50(5):05FD03.
- [33] K. Mimura, Y. Taguchi, S. Fukuda, A. Mitsuda, J. Sakurai, K. Ichikawa, and O. Aita, Temperature dependence of Eu 4f states in EuPd_2Si_2 : bulk-sensitive high-resolution photoemission study, *Physica B: Condensed Matter* (2004), 351(3-4):292-294.
- [34] H. Wada, A. Mitsuda, M. Shiga, H. A. Katori, and T. Goto, First-order valence transition of EuPd_2Si_2 induced by high magnetic fields, *Journal of the Physical Society of Japan* (1996), 65(11), 3471-3473.
- [35] G. Renaud, A. Barbier, and O. Robach, Growth, structure, and morphology of the Pd/MgO(001) interface: Epitaxial site and interfacial distance, *Physical Review B* (1999), 60(8):5872-5882.